photochem

MDPI

Article

g-C_3N_4/MoS_2 Heterojunction for Photocatalytic Removal of Phenol and Cr(VI)

Ilaeira Rapti [1], Feidias Bairamis [1] and Ioannis Konstantinou [1,2,*]

[1] Department of Chemistry, University of Ioannina, 45100 Ioannina, Greece; il_rapti@windowslive.com (I.R.); bairamisfeidias@gmail.com (F.B.)
[2] Institute of Environment and Sustainable Development, University Research Center of Ioannina (URCI), 45110 Ioannina, Greece
* Correspondence: iokonst@uoi.gr

Abstract: In this study, molybdenum disulfide (MoS_2) decorated on graphitic carbon nitride (g-C_3N_4) heterostructure catalysts at various weight ratios (0.5%, 1%, 3%, 10%, *w*/*w*) were successfully prepared via a two-step hydrothermal synthesis preparation method. The properties of the synthesized materials were studied by X-ray diffraction (XRD), attenuated total reflectance–Fourier transform infrared spectroscopy (ATR-FT-IR), UV–Vis diffuse reflection spectroscopy (DRS), scanning electron microscopy (SEM) and N_2 porosimetry. MoS_2 was successfully loaded on the g-C_3N_4 forming heterojunction composite materials. N_2 porosimetry results showed mesoporous materials, with surface areas up to 93.7 m^2g^{-1}, while determined band gaps ranging between 1.31 and 2.66 eV showed absorption over a wide band of solar light. The photocatalytic performance was evaluated towards phenol oxidation and of Cr(VI) reduction in single and binary systems under simulated sunlight irradiation. The optimum mass loading ratio of MoS_2 in g-C_3N_4 was 1%, showing higher photocatalytic activity under simulated solar light in comparison with bare g-C_3N_4 and MoS_2 for both oxidation and reduction processes. Based on scavenging experiments a type-II photocatalytic mechanism is proposed. Finally, the catalysts presented satisfactory stability (7.8% loss) within three catalytic cycles. Such composite materials can receive further applications as well as energy conversion.

Keywords: C_3N_4; MoS_2; composite; photocatalytic oxidation; Cr(VI) reduction

Citation: Rapti, I.; Bairamis, F.; Konstantinou, I. g-C_3N_4/MoS_2 Heterojunction for Photocatalytic Removal of Phenol and Cr(VI). *Photochem* **2021**, *1*, 358–370. https://doi.org/10.3390/photochem1030023

Academic Editor: Vincenzo Vaiano

Received: 22 September 2021
Accepted: 12 October 2021
Published: 15 October 2021

1. Introduction

Energy crisis and environmental pollution are currently among the most serious problems for humans [1]. Emerging and priority environmental pollutants comprise several chemical categories such as pharmaceuticals, pesticides and plasticizers. Phenol and in general phenolics may be present in several wastewater streams from different production processes as well as degradation products from the previously mentioned pollutants. In addition, toxic metal ions such as Cr(VI) may be present in combined wastewater streams; thus, treatment methods should be capable of removing both organic and inorganic pollutants. However, conventional treatment methods present either low removal of certain organic pollutants or are incapable of simultaneous removal of organics and toxic metal ions [2]. Therefore, there has been an increased interest in the development of more efficient and environmentally friendly methods for the removal of pollutants from wastewater, and for this reason the advanced oxidation processes (AOPs) are widely used. Their effectiveness for organics removal is based on the production of hydroxyl radicals, which are powerful oxidizing agents. Heterogeneous photocatalysis, which presents advantages over other removal techniques as it can be applied for both oxidation and reduction of pollutants in ambient conditions in the presence of solar radiation and for organic pollutants, can lead to complete mineralization [2–6].

Graphitic carbon nitride (g-C_3N_4) has drawn widespread attention and become a hotspot in various scientific disciplines as a metal-free semiconductor due to its advantages. It has an appealing electronic structure with a 2.7 eV band gap, it can be fabricated with low-cost precursors (e.g., urea, thiourea, melamine) [3,7,8] and it is environmentally friendly. However, the rapidly photogenerated electron–hole recombination diminishes the photocatalytic efficiency. The coupling of g-C_3N_4 with other semiconductors with an appropriate band gap was considered to increase photocatalytic efficiency.

Molybdenum sulfide (MoS_2) has attracted attention as an emerging photocatalytic cocatalyst material due to its distinctive features, such as high stability and hardness, reliability, non-toxicity and low cost. It possesses a narrow band gap (1.2–1.9 eV), which offers a wide spectral absorption range and provides high speed channels for the interfacial charge transfer in heterostructures [3]. Previous studies have explored the application of MoS_2 in Cr(VI) reduction. Photoreduction and chemical reduction (redox between MoS_2 and Cr(VI)) were determined through a collaborative contribution to reducing Cr(VI) by MoS_2 under light conditions [9–11]. The coupling of two semiconductors (MoS_2, g-C_3N_4) could significantly reduce the charge carrier recombination and highly improve photocatalytic activity compared to those bare materials. MoS_2/g-C_3N_4 has been synthesized and tested for energy conversion, as a supercapacitor and for organic dye degradation [3,12–15]; however, its application to the simultaneous oxidation/reduction of environmental pollutants has not been studied so far.

Based on the above, the present study deals with the preparation of a series of MoS_2/g-C_3N_4 heterostructure composite catalysts and their application for the removal of phenol and Cr(VI) for aqueous solutions. There are few works exploring the synthesis of MoS_2/g-C_3N_4 heterojunction structure via various methods such as hydrothermal treatment, impregnation-sulfidation and photodeposition [16–19]. Here, a two-step hydrothermal synthesis combined with a sonication–liquid exfoliation preparation method is proposed.

2. Materials and Methods

2.1. Materials and Chemicals

Urea (99.5%, M_w: 60.06 gmol^{-1}), thiourea (>99%, M_w: 76.12 gmol^{-1}) and 1,5-diphenyl carbazide (98% (M_w: 242.28) were obtained from Acros Organics (Geel, Belgium). Ammonium molybdate tetrahydrate (99%, M_w: 1235.86 gmol^{-1}) was supplied by Janssen Chimica. Potassium dichromate (KCr_2O_7, M_w: 294.18 gmol^{-1}) was obtained from Sigma-Aldrich (St. Louis, MO, USA). Phenol (M_w: 94.11 gmol^{-1}) was purchased by Merck kGaA (Darmstadt, Germany). Methanol (MeOH), sulfuric acid >95% (H_2SO_4), methanol HPLC grade (MeOH, M_w: 32.04 gmol^{-1}) and water HPLC grade (M_w: 18.02 gmol^{-1}) were supplied by Fischer Scientific (Loughborough, Leics, UK). Distilled water was used throughout the experimental procedures of the study.

2.2. Preparation of g-C_3N_4, MoS_2 and Composite MoS_2/g-C_3N_4 Photocatalysts

2.2.1. Synthesis of Bare Carbon Nitride (g-C_3N_4) and Molybdenum Disulfide (MoS_2)

Graphitic carbon nitride (g-C_3N_4) was synthesized by thermal treatment of urea as a precursor compound. In a typical synthesis of g-C_3N_4, 30 g of urea was put in a crucible. After being dried at 90 °C it was heated to 500 °C at a heating rate of 10 °C/min and kept at this temperature for 4 h. The resulting yellow powder was collected and ground into a powder.

Molybdenum disulfide was prepared by hydrothermal synthesis. Hexaammonium heptamolybdate tetrahydrate and thiourea were dissolved in 10 mL of deionized water by stirring for 1 h at room temperature. The resulting solution was then placed in a Teflon-lined autoclave reactor and heated in an oven at 200 °C for 12 h.

2.2.2. Synthesis of MoS_2/g-C_3N_4 Heterostructure

MoS_2/g-C_3N_4 heterostructures with 0.5%, 1%, 3%, 10% (wt%) ratios were synthesized. An appropriate amount of bulk g-C_3N_4 was added in isopropanol into a beaker, and the mixture was sonicated for 2 h at room temperature. In a separate beaker, MoS_2 nanoparticles was added in a water/isopropanol (2:1) solution, and the mixture was sonicated for 2 h at room temperature. The solutions were mixed together and sonicated for another 2 h at room temperature. The product was cleaned with water and ethanol, collected by centrifuging and dried at 60 °C [18]. Then it was calcinated in air at 200 °C for 4 h.

2.3. Material Characterization

The crystal forms of the photocatalysts were analyzed from their X-ray diffraction (XRD) patterns using a Bruker Advance D8 X-ray powder diffractometer (Billerica, MA, USA) working with Cu-K_a (λ = 1.5406 Å) radiation. Diffractograms were scanned from 2θ 10° to 90°. The patterns were assigned to crystal phases with the use of the International Center for Diffraction Data (ICCD).

Attenuated total reflectance–Fourier transform infrared spectroscopy (ATR-FT-IR) was conducted to characterize the functional groups of different catalysts. A Shimadzu IR Spirit-T spectrophotometer (Kyoto, Japan) with a QATR-S single-reflection ATR measurement attachment equipped with diamond prism was used. The photocatalysts were scanned in the range 4000–400 cm^{-1}.

The UV–Vis diffuse reflectance spectra (DRS) of the catalyst powders were recorded using a Shimadzu 2600 spectrophotometer bearing an IRS-2600 integrating sphere (Kyoto, Japan) in the wavelength of 200–800 nm at room temperature using $BaSO_4$ (Nacalai Tesque, extra pure reagent, Kyoto, Japan) as a reference sample.

The morphology of the catalysts was examined by scanning electron microscopy (SEM) using a JEOL JSM 5600 (Tokyo, Japan) working at 20 kV.

Nitrogen adsorption–desorption isotherms were collected by porosimetry using a Quantachrome Autosorb-1 instrument (Bounton Beach, FL, USA) at 77K. The samples (≈80 mg) were degassed at 150 °C for 3 h. The Brunauer–Emmet–Teller (BET) method was used to calculate the specific area (SSA) of each material at relative pressure between 0.05 and 0.3. The adsorbed amount of nitrogen at relative pressure P/P_0 = 0.95 was used in order to calculate the total pore volume (V_{TOT}). The Barrett, Joyner and Halenda (BJH) method was used to determine the pore size distribution (PSD) of the photocatalysts.

2.4. Photocatalytic Experiments

Photocatalytic experiments were carried out using Atlas Suntest XLS+ (Atlas, Germany) solar simulator apparatus equipped with a xenon lamp (2.2 kW) and special filters in place to prevent the transmission of wavelengths below 290 nm. During the experiments the irradiation intensity was maintained at 500 W m^{-2}.

Aqueous solutions (100 mL) and the catalyst (10 mg) were transferred into a double-walled Pyrex glass reactor, thermostated by water flowing in the double-skin of the reactor. In binary systems the pH was adjusted to ca. 2 with sulfuric acid in order to achieve high adsorption efficiency of Cr(VI) onto the catalysts and avoid $Cr(OH)_3$ deposition on the catalyst surface, based on previous studies [11,20]. Before exposure to light, the suspension was stirred in the dark for 30 min to ensure the establishment of adsorption–desorption equilibrium onto the catalyst surface. The obtained aliquot (5 mL) was withdrawn at different time intervals and was filtered through 0.45 μm filters in order to remove the catalyst's particles before further analysis. Quantification of phenol for the kinetic studies in aquatic solutions was carried out by high performance liquid chromatography (HPLC) (Schimadzu, LC 10AD, Diode Array Detector SPD-M10A, Degasser DGU-14A). The column oven (Schimadzu, CTO-10A) was set at 40 °C. The mobile phase used was a mixture of water HPLC grade (50%) and methanol HPLC grade (50%). The concentration of Cr(VI)

was determined by the diphenylcarbazide colorimetric method measuring the absorbance at the wavelength of 540 nm using a UV–Vis spectrophotometer (Jasco-V630, Tokyo, Japan).

3. Results and Discussion

3.1. Characterization of the Prepared Photocatalysts

3.1.1. Structural Characterization

The XRD patterns for g-C_3N_4, MoS_2 and MoS_2/g-C_3N_4 composites are shown in Figure 1. For g-C_3N_4 two characteristic intense peaks were observed at 13.1° and 27.4°. A broad peak was observed corresponding to the (100) plane, arising from in-plane stacking of the tri-s-triazine motif, and to the (002) interlayer stacking of the conjugated aromatic rings. For MoS_2 three characteristic intense peaks at 13.4°, 33.5° and 57.8° were observed, which can be indexed to the (002), (100) and (110) planes, respectively, corresponding to the hexagonal phase of MoS_2 (JCPDS 87-1526) [21–24].

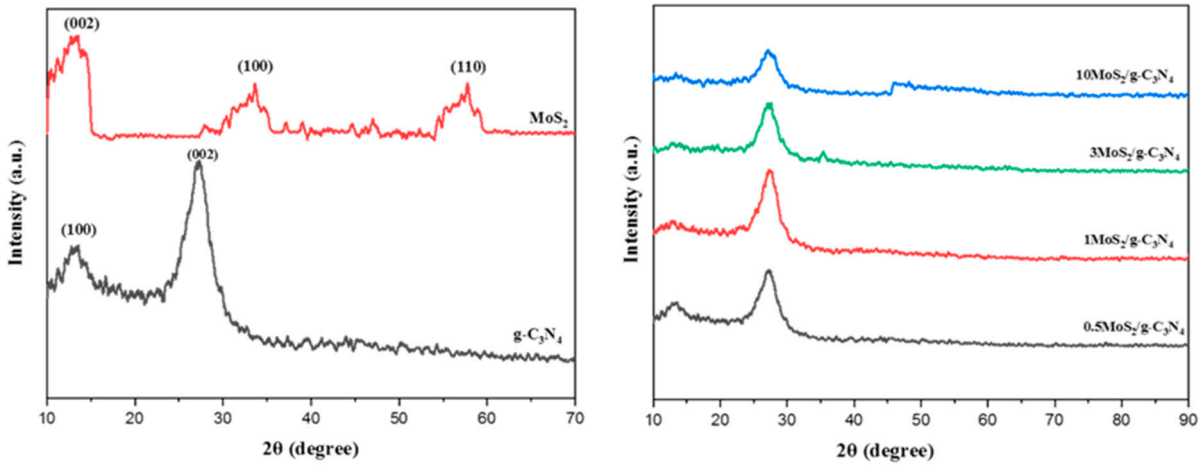

(**a**) (**b**)

Figure 1. XRD patterns of (**a**) g-C_3N_4, MoS_2, (**b**) composite catalysts.

For the prepared composite catalysts no diffraction peaks corresponding to MoS_2 can be recognized, which may be because of the small quantity of MoS_2 contents and high dispersion in g-C_3N_4 photocatalysts.

The ATR-FT-IR spectra of g-C_3N_4, MoS_2 and g-C_3N_4/MoS_2 composite are shown in Figure 2. The prepared catalysts presented the main characteristic peaks of both g-C_3N_4 and MoS_2 suggesting the formation of composite heterostructures. The peaks of g-C_3N_4 can be observed at 1573, 1465, 1403, 1319 and 1241 cm^{-1} confirming the stretching vibration of C–N (–C)–C or C–NH–C heterocycles. The broad peaks between 3300 and 3000 cm^{-1} are related to the stretching vibration of N-H, and the peak at 1637 cm^{-1} corresponds to the C=N bending vibration. The peak at 810 cm^{-1} corresponds to heptazine ring vibration. The peak at 1400 cm^{-1} confirms the presence of amino groups. The peaks of MoS_2 can be observed at 689 cm^{-1}, confirming the stretching vibration of Mo–O. The peak at 1112 cm^{-1} corresponds to the stretching vibration of S=O [25].

3.1.2. Morphology Surface Analysis

The morphological evaluation of all catalysts was carried out by scanning electron microscopy (Figure 3). Figure 3a shows the morphology of g-C_3N_4 consisting of packed sheets. Figure 3b presents aggregation of flower-like spherical particles of MoS_2 [26]. Figure 3c (1MoS_2/g-C_3N_4) shows a morphology that seems to be close to that of g-C_3N_4; this may be because of the small quantity of MoS_2 contents on the surface of g-C_3N_4. The 10MoS_2/g-C_3N_4 (Figure 3d) reveals MoS_2 spheres attached on the surface of the g-C_3N_4 sheets.

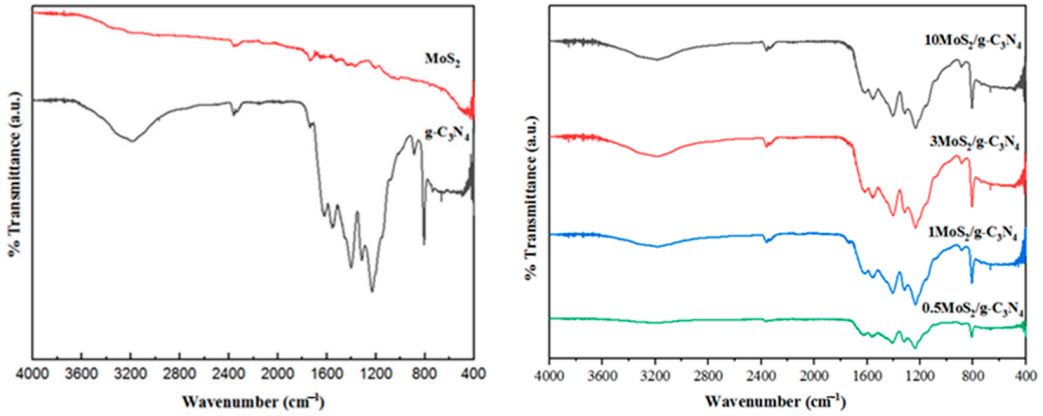

(**a**) (**b**)

Figure 2. ATR-FT-IR spectra of (**a**) g-C_3N_4, MoS_2, (**b**) composite catalysts.

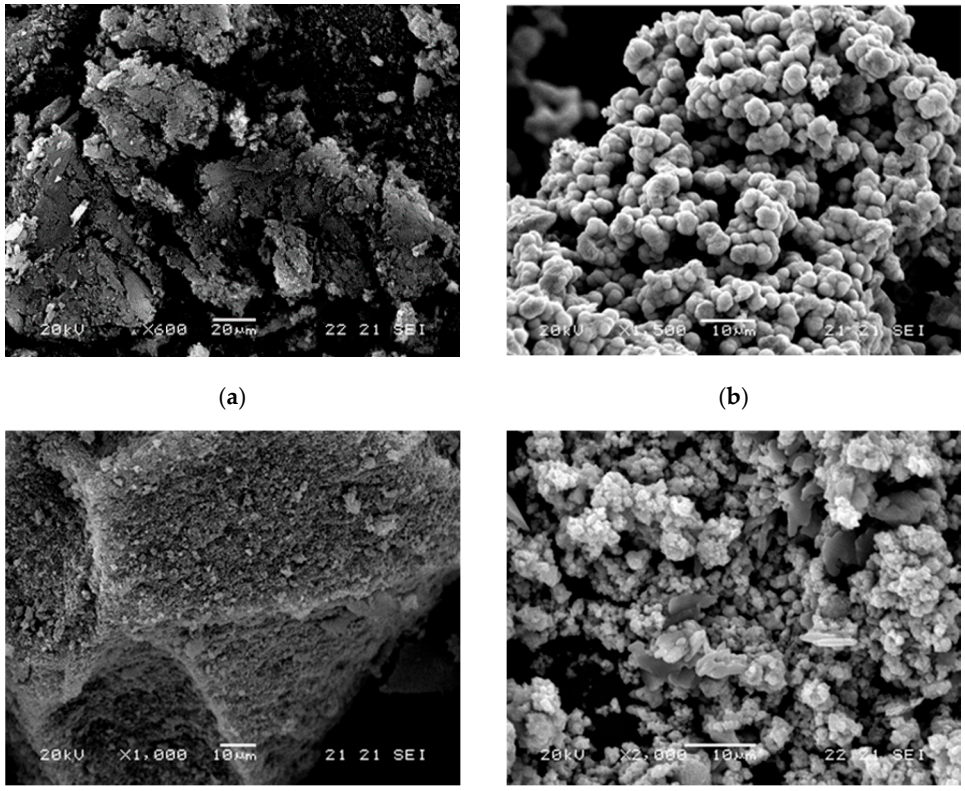

(**a**) (**b**)

(**c**) (**d**)

Figure 3. SEM images of (**a**) g-C_3N_4, (**b**) MoS_2 and (**c**) 1MoS_2/g-C_3N_4 and (**d**) 10MoS_2/g-C_3N_4.

The nitrogen adsorption–desorption isotherms for the prepared photocatalysts are presented in Figure 4.

All composites samples exhibited typical type IV(a) adsorption and desorption isotherms with H3 hysteresis loop according to the IUPAC classification, suggesting mesoporous materials [27]. BET specific surface area ranged between 2.0 m^2g^{-1} for MoS_2 and 93.7 m^2g^{-1} for g-C_3N_4. MoS_2 presented a non-porous structure with some porosity owed to the aggregation of spherical particles. The calculated specific surface area, average pore diameter and total pore volume of the catalysts are shown in Table 1.

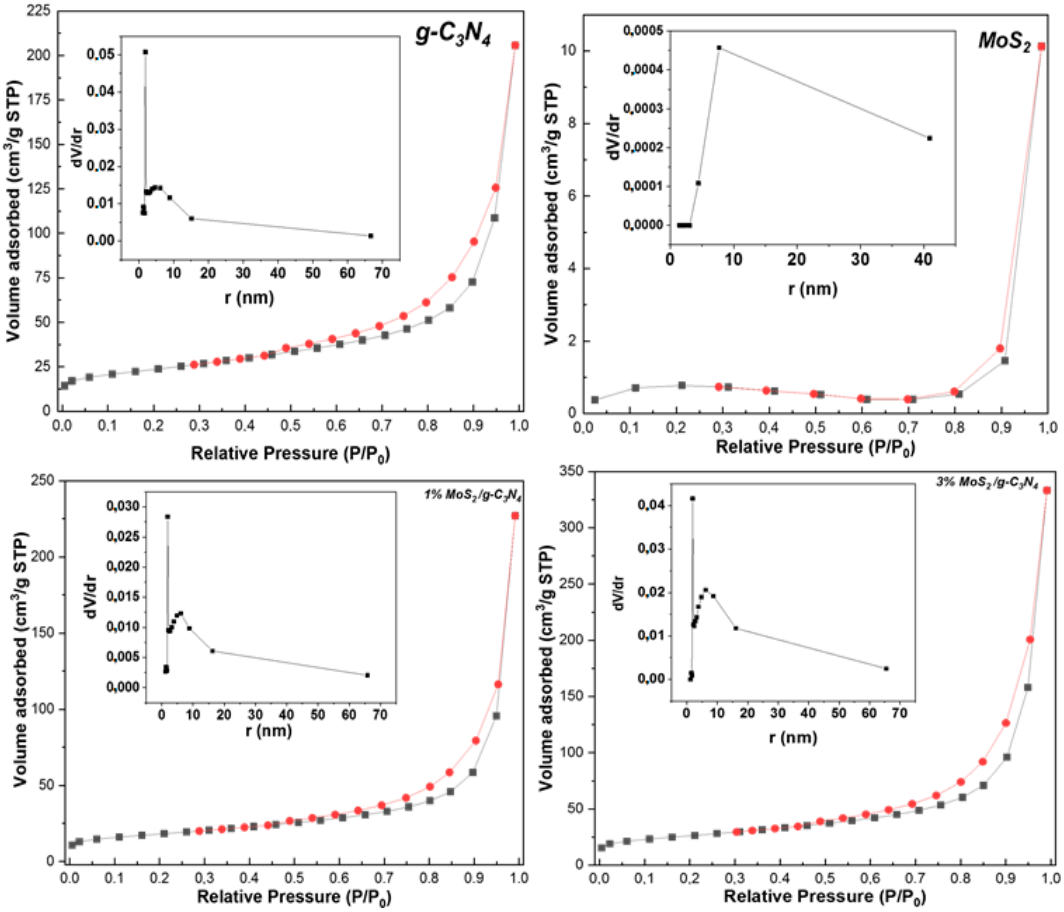

Figure 4. Nitrogen adsorption–desorption isotherms and pore size distributions for g-C_3N_4, MoS_2, 1MoS_2/g-C_3N_4, 3MoS_2/g-C_3N_4.

Table 1. Specific surface area, average pore diameter and total pore volume of prepared catalysts.

Catalyst	Specific Surface Area S_{BET} (m^2g^{-1})	Average Pore Diameter (nm)	V_{TOT} (cm^3 g^{-1})
MoS_2	2.0	31	0.016
g-C_3N_4	81.3	8.3	0.169
0.5% MoS_2/g-C_3N_4	93.7	10.2	0.238
1% MoS_2/g-C_3N_4	62.2	9.5	0.148
3% MoS_2/g-C_3N_4	90.2	10.9	0.245
10% MoS_2/g-C_3N_4	92.1	10.5	0.239

3.1.3. UV–Vis Spectroscopy and Band Gap Determination

The diffuse reflectance spectroscopy (DRS) results and the energy band gap (E_g), calculated with the Kübelka–Munk function, of all photocatalysts are presented in Figure 5. The absorption edge of MoS_2 was determined at 946 nm, while the absorption edge of g-C_3N_4 was at 480 nm indicating visible light response. The absorption edges of the prepared composite catalysts varied between 466–946 nm and the energy band gap 1.31–2.66 eV. The band gap energy and corresponding absorption edges are shown in Table 2.

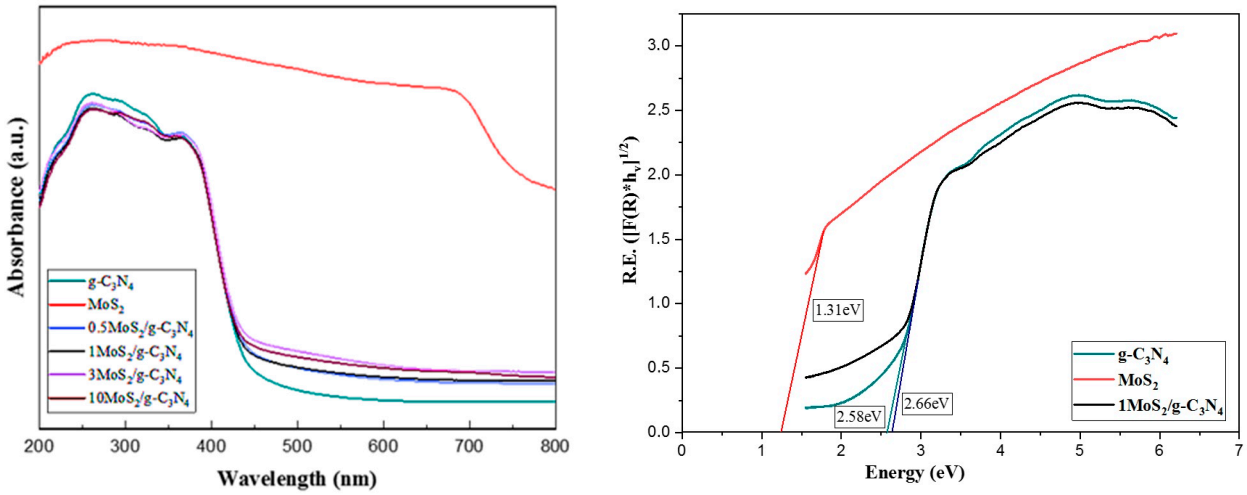

(**a**) (**b**)

Figure 5. (**a**) UV–Vis absorption spectra of prepared catalysts, (**b**) Kübelka–Munk plots for g-C_3N_4, MoS_2 and 1MoS_2/g-C_3N_4 for indirect band gap semiconductors.

Table 2. Energy band gap and absorption edge of prepared catalysts.

Catalyst	Energy Band Gap (eV)	Absorption Edge λ (nm)
g-C_3N_4	2.58	480
MoS_2	1.31	946
0.5% MoS_2/g-C_3N_4	2.56	484
1% MoS_2/g-C_3N_4	2.66	466
3% MoS_2/g-C_3N_4	2.64	469
10% MoS_2/g-C_3N_4	2.64	469

MoS_2/g-C_3N_4 heterojunction samples presented enhanced light absorption in the visible region as compared to g-C_3N_4. The absorption intensity of the prepared samples strengthened with increasing MoS_2 contents, which agrees with the color of the prepared samples that vary from light yellow to grey.

The band edge position of conduction band (CB) and valence band (VB) of prepared catalysts was determined applying Equations (1) and (2).

$$E_{VB} = X - E_0 + 0.5E_g \quad (1)$$

$$E_{CB} = E_{VB} - E_g \quad (2)$$

where E_{VB} is the VB edge potential, E_{CB} is the CB edge potential, E_g is the band gap energy of the catalysts, X is the electronegativity of g-C_3N_4 (4.67 eV) and MoS_2 (5.33 eV) [28] and E_0 is the energy of free electrons on the hydrogen scale (4.5 eV). The E_{VB} and E_{CB} of g-C_3N_4 was calculated at 1.46 and −1.12 eV, respectively, while for MoS_2 the corresponding values were 1.48 and 0.17 eV.

3.2. Photocatalytic Study

The photocatalytic performance of composite catalysts was studied against the oxidation of phenol (single system: C_{ph} = 10 mg L^{-1}, C_{cat} = 100 mg L^{-1}) as well as the simultaneous photocatalytic reduction of Cr(VI) and oxidation of phenol (binary system: phenol/Cr(VI) = 1/10, C_{cat} = 100 mg L^{-1}, pH = 2 [29,30]) under simulated sunlight irradiation. The results of all photocatalytic experiments are shown in Figure 6 and Tables 3 and 4.

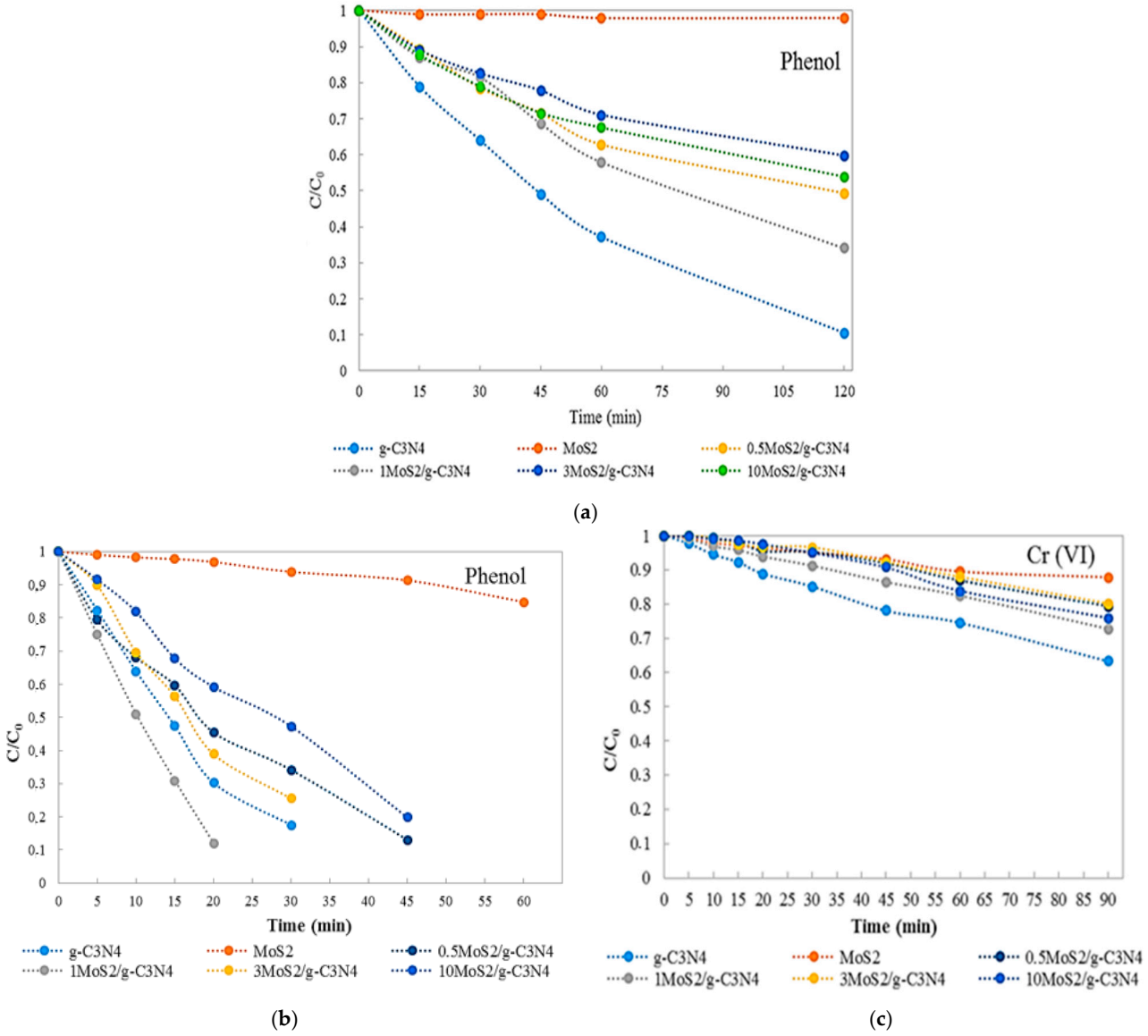

Figure 6. Photocatalytic degradation kinetics of (**a**) phenol in single system, (**b**) phenol and (**c**) Cr(VI) in binary system under solar light irradiation.

Table 3. Kinetic parameters (first-order kinetic constants (k), half-life ($t_{1/2}$) and correlation coefficients (R^2) of phenol in single system.

Catalyst	k (min^{-1})	$t_{1/2}$ (min)	R^2
$g\text{-}C_3N_4$	0.022	31.5	0.9401
MoS_2	0.0002	3465.0	0.5016
$0.5MoS_2/g\text{-}C_3N_4$	0.006	116.0	0.9528
$1MoS_2/g\text{-}C_3N_4$	0.009	77.0	0.9940
$3MoS_2/g\text{-}C_3N_4$	0.005	139.0	0.9250
$10MoS_2/g\text{-}C_3N_4$	0.006	116.0	0.9158

The first-order apparent reaction rates for phenol photocatalytic degradation in single system follows the sequence $k_{g\text{-}C_3N_4} > k_{1MoS_2/g\text{-}C_3N_4} > k_{0.5MoS2/g\text{-}C3N4} > k_{10MoS_2/g\text{-}C_3N_4} > k_{3MoS_2/g\text{-}C_3N_4} > k_{MoS_2}$. In the binary system, reaction rates of phenol oxidation were as follows: $k_{1MoS_2/g\text{-}C_3N_4} > k_{g\text{-}C_3N_4} > k_{3MoS_2/g\text{-}C_3N_4} > k_{0.5MoS_2/g\text{-}C_3N_4} > k_{10MoS_2/g\text{-}C_3N_4} > k_{MoS_2}$, and as to the reduction of Cr(VI) it was as follows: $k_{g\text{-}C_3N_4} > k_{1MoS_2/g\text{-}C_3N_4} > k_{10MoS_2/g\text{-}C_3N_4} > k_{0.5MoS_2/g\text{-}C_3N_4} > k_{3MoS_2/g\text{-}C_3N_4} > k_{MoS_2}$.

In comparison, the prepared catalysts exhibit faster kinetics of phenol and Cr(VI) removal in binary than in single systems.

Table 4. Kinetic parameters (first-order kinetic constants (k), half-life ($t_{1/2}$) and correlation coefficients (R^2)) of phenol and Cr(VI) in binary system.

Binary	Phenol			Cr(VI)		
Catalyst	**k (min^{-1})**	**$t_{1/2}$ (min)**	**R^2**	**k (min^{-1})**	**$t_{1/2}$ (min)**	**R^2**
g-C_3N_4	0.068	10.2	0.9978	0.003	231.0	0.9477
MoS_2	0.002	346.5	0.9373	0.002	346.5	0.9694
0.5MoS_2/g-C_3N_4	0.042	16.5	0.9738	0.002	346.5	0.9552
1MoS_2/g-C_3N_4	0.091	7.6	0.9246	0.003	231.0	0.9740
3MoS_2/g-C_3N_4	0.042	16.5	0.9513	0.002	346.5	0.9478
10MoS_2/g-C_3N_4	0.031	22.4	0.9374	0.003	231.0	0.9325

3.3. Photocatalytic Mechanism for the Composite Photocatalysts

Different photoinduced reactive species, such as hydroxyl radicals (OH·), superoxide radicals (O_2^-) and holes (h^+), may be involved in the photocatalytic process after electron–hole pairs are generated. Thus, photocatalytic experiments in the presence of isopropanol (IPA), superoxide dismutase (SOD) and triethanolamine (TEOA) were used to scavenge $^{\bullet}OH$, O_2^- and h^+, respectively, during the photodegradation of phenol in order to investigate the photocatalytic mechanism [3]. As shown in Table 5, the degradation rate constant (k) for phenol was 0.009 min^{-1} after exposure for 120 min under simulated sunlight without scavenger addition, and this changed after adding, IPA, SOD and TEOA, to 0.003, 0.004 and 0.002 min^{-1}, respectively. It is clearly observed that the degradation of phenol was inhibited with the addition of scavengers, though TEOA was the most obvious. The degradation kinetics of phenol in the presence of scavengers are shown in Figure 7 and Table 5.

Table 5. Kinetic parameters (first-order kinetic constants (k), half-life ($t_{1/2}$) and correlation coefficients (R^2)) of phenol in scavenging experiments.

Scavenger	k (min^{-1})	$t_{1/2}$ (min)	R^2
IPA	0.003	231	0.9742
SOD	0.004	173.2	0.9590
TEOA	0.002	346.5	0.9553
no scavenger	0.009	77.0	0.9940

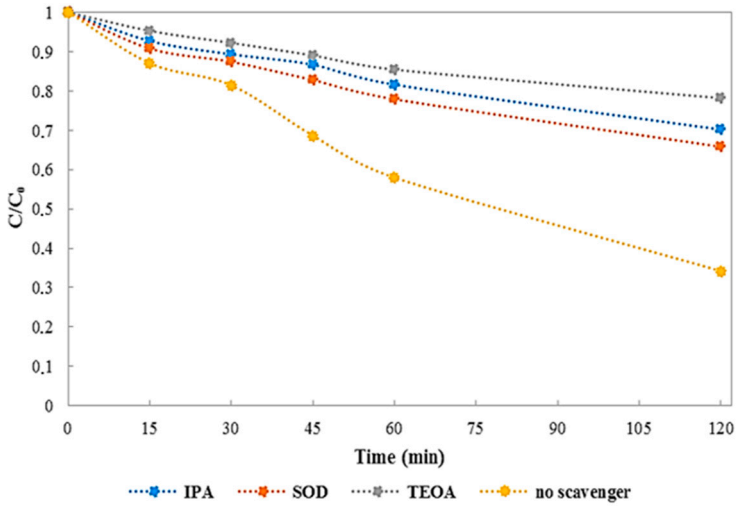

Figure 7. Photocatalytic degradation kinetics of phenol in single system in the presence of scavengers and 1MoS_2/g-C_3N_4 photocatalyst under solar light irradiation.

According to the above analysis, the proposed photocatalytic mechanism (Type II), involving the carrier transfer and photodegradation of phenol was illustrated as shown in Figure 8. The photogenerated electron–hole pairs were induced in the conduction band (CB) and valence band (VB) of g-C_3N_4 and MoS_2 under irradiation. The photogenerated electrons transferred from the CB of g-C_3N_4 to that of MoS_2, while holes moved from the VB of MoS_2 to that of g-C_3N_4, leading the photogenerated electron–hole pair to be separated and transferred effectively. The holes (h^+) in the VB of g-C_3N_4 participate in the degradation process. Simultaneously, electrons (e^-) in the CB together with H^+ can reduce O_2 to H_2O_2, which forms hydroxyl radicals. The e^- on the CB of g-C_3N_4 and MoS_2 participates in the reduction of Cr(VI) to Cr(III). The proposed mechanism provides additional explanation for the better removal performance in the binary system. Regarding the reduction process, the electrons on MoS_2 have weaker reduction ability; consequently they can reduce strong oxidation agents such as Cr(VI), enhancing the target reduction reaction without other reactions, such as O_2 reduction. As far as the oxidation pathway is concerned, the enhancement is due to the better charge separation. The results of the present study indicate that the MoS_2 could be a promising candidate as a non-noble metal co-catalyst for g-C_3N_4 photocatalysts. The composite catalysts can receive further applications either for degradation of pollutants or in energy conversion.

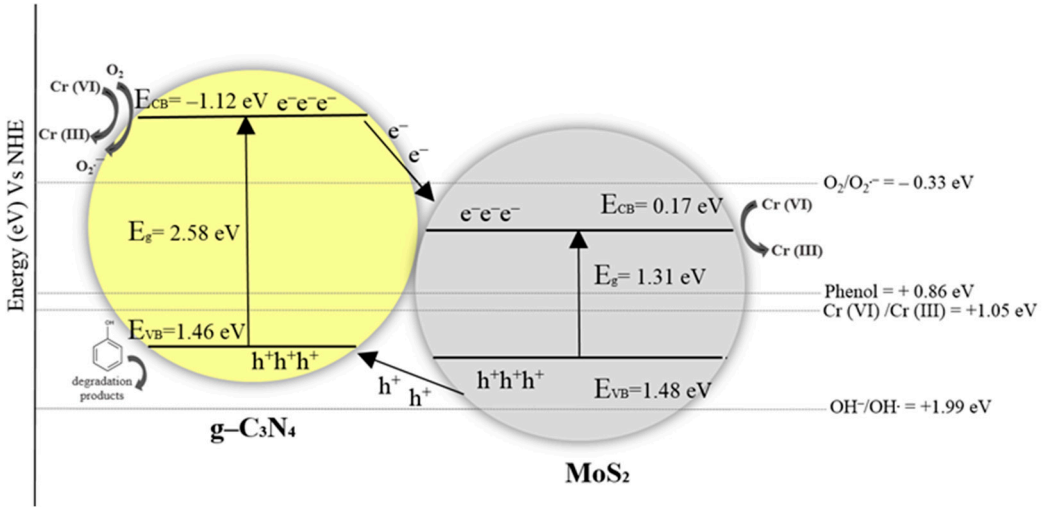

Figure 8. Schematic illustration of carrier transfer in the MoS_2/g-C_3N_4 heterojunction.

3.4. Recyclability of the Composite Photocatalysts

The stability of the prepared photocatalysts was investigated by examining the photocatalytic activity of the most efficient photocatalyst (1MoS_2/g-C_3N_4) against oxidation of phenol in binary system for three continuous cycles (Figure 9). Reaction constants of phenol oxidation were 0.090, 0.089 and 0.083 min^{-1} for the first, second and third cycle, respectively (Table 6). A total loss of photocatalytic activity about 7.8% after the third photocatalytic cycle showed the sufficient stability of the catalyst considering also the possible losses of catalyst particles during the recovery process after each cycle. In addition, the catalyst separated at the end of the third catalytic cycle was characterized by XRD, SEM and ATR-FT-IR (Figure 10a–c), revealing a nearly identical pattern to the starting material.

Table 6. Kinetic parameters (first-order kinetic constants (k), half-life ($t_{1/2}$) and correlation coefficients (R^2)) of phenol degradation by 1MoS_2/g-C_3N_4 catalyst after three consecutive cycles.

Cycle	k (min^{-1})	$t_{1/2}$ (min)	R^2
1	0.09	7.7	0.9510
2	0.089	7.8	0.9453
3	0.083	8.3	0.9496

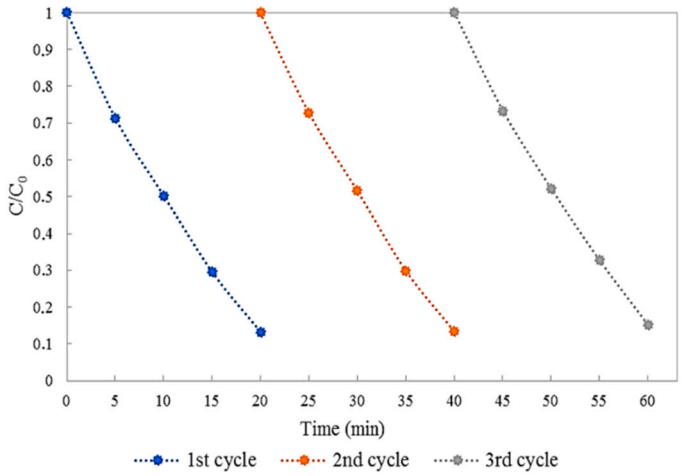

Figure 9. Reusability performance of $1MoS_2/g\text{-}C_3N_4$ photocatalyst for three continuous cycles.

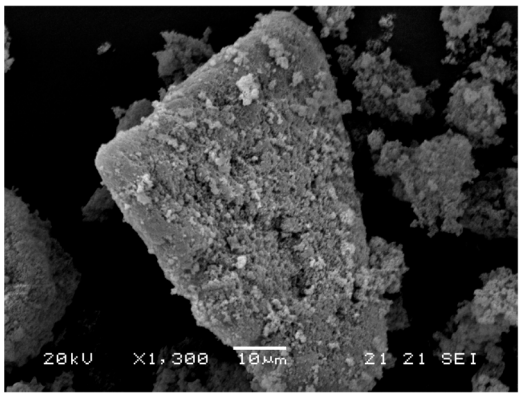

(**a**)

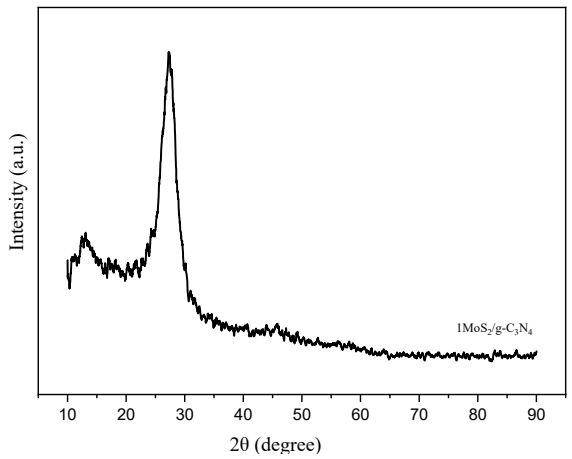

(**b**)

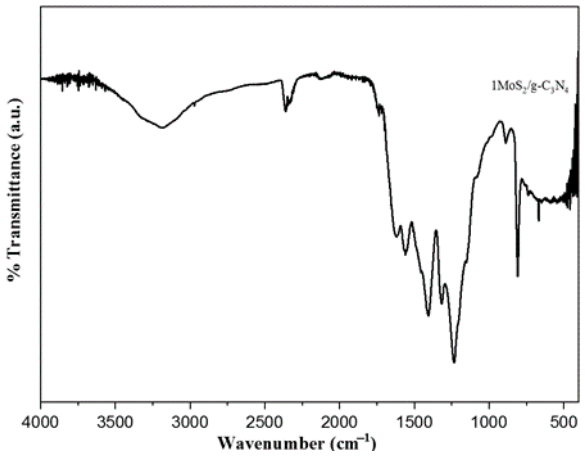

(**c**)

Figure 10. (**a**) SEM image, (**b**) XRD pattern, (**c**) ATR-FT-IR spectra of $1MoS_2/g\text{-}C_3N_4$ photocatalyst after the third photocatalyst cycle.

4. Conclusions

In this work, mesoporous $MoS_2/g\text{-}C_3N_4$ heterostructures were successfully synthesized via a two-step hydrothermal synthesis at various weight ratios (up to 10% *w*/*w* of MoS_2) and assayed for the simultaneous oxidation of phenol and Cr(VI) reduction. Composite materials show higher photocatalytic activity under solar light in comparison with bare $g\text{-}C_3N_4$ and MoS_2 for both oxidation and reduction processes, while the material with 1% MoS_2 loading was found as the catalyst with the best efficiency. A considerable

enhancement of the photocatalytic efficiency was observed for the binary system compared to the single component systems, indicating a promoting synergistic effect. The three cycling experiments indicated that the catalysts presented a good stability. Finally, type-II band alignment was proposed as the photocatalytic mechanism for the composed catalysts.

Author Contributions: Conceptualization, I.R. and I.K.; methodology, I.R. and I.K.; formal analysis, I.R. and F.B.; investigation, I.R. and I.K.; resources, I.K.; data curation, I.R.; writing—original draft preparation, I.R. and I.K.; writing—review and editing I.K., I.R. and F.B.; visualization, I.R.; supervision, I.K.; project administration, I.R.; funding acquisition, I.K. All authors have read and agreed to the published version of the manuscript.

Funding: This research received no external funding.

Institutional Review Board Statement: Not applicable.

Informed Consent Statement: Not applicable.

Data Availability Statement: Not applicable.

Acknowledgments: The authors acknowledge the access in XRD and SEM units of the University of Ioannina. The authors would like to thank D. Petrakis for the collaboration in the Laboratory of Industrial Chemistry, Dept. of Chemistry, University of Ioannina.

Conflicts of Interest: The authors declare no conflict of interest.

References

1. Jiménez-Rangel, K.Y.; Lartundo-Rojas, L.; García-García, A.; Cipagauta-Díaz, S.; Mantilla, A.; Samaniego-Benítez, J.E. Hydrothermal Synthesis of a Two-Dimensional g-C_3N_4/MoS_2/MnOOH Composite Material and Its Potential Application as Photocatalyst. *J. Chem. Technol. Biotechnol.* **2019**, *94*, 3447–3456. [CrossRef]
2. Antonopoulou, M.; Giannakas, A.; Konstantinou, I. Simultaneous Photocatalytic Reduction of Cr(VI) and Oxidation of Benzoic Acid in Aqueous N-F-Codoped TiOsuspensions: Optimization and Modeling Using the Response Surface Methodology. *Int. J. Photoenergy* **2012**, *1*, 358–370. [CrossRef]
3. Zhang, X.; Zhang, R.; Niu, S.; Zheng, J.; Guo, C. Enhanced Photo-Catalytic Performance by Effective Electron-Hole Separation for MoS_2 Inlaying in g-C_3N_4 Hetero-Junction. *Appl. Surf. Sci.* **2019**, *475*, 355–362. [CrossRef]
4. Cuerda-Correa, E.M.; Alexandre-Franco, M.F.; Fernández-González, C. Advanced Oxidation Processes for the Removal of Antibiotics from Water. An Overview. *Water* **2020**, *12*, 102. [CrossRef]
5. Barrera-Díaz, C.; Cañizares, P.; Fernández, F.J.; Natividad, R.; Rodrigo, M.A.; Rosedal, E.; Toluca, E.; de México, M. Electrochemical Advanced Oxidation Processes: An Overview of the Current Applications to Actual Industrial Effluents. *J. Mex. Chem. Soc.* **2014**, *58*, 3. [CrossRef]
6. Malato, S.; Fernández-Ibáñez, P.; Maldonado, M.I.; Blanco, J.; Gernjak, W. Decontamination and Disinfection of Water by Solar Photocatalysis: Recent Overview and Trends. *Catal. Today* **2009**, *147*, 1–59. [CrossRef]
7. Zhang, G.; Zhang, J.; Zhang, M.; Wang, X. Polycondensation of Thiourea into Carbon Nitride Semiconductors as Visible Light Photocatalysts. *J. Mater. Chem.* **2012**, *22*, 8083–8091. [CrossRef]
8. Bairamis, F.; Konstantinou, I. WO3 Fibers/g-C_3N_4 Z-Scheme Heterostructure Photocatalysts for Simultaneous Oxidation/Reduction of Phenol/Cr(VI) in Aquatic Media. *Catalysts* **2021**, *11*, 792. [CrossRef]
9. Sun, K.; Jia, F.; Yang, B.; Lin, C.; Li, X.; Song, S. Synergistic Effect in the Reduction of Cr(VI) with Ag-MoS_2 as Photocatalyst. *Appl. Mater. Today* **2020**, *18*, 100453. [CrossRef]
10. Sun, H.; Wu, T.; Zhang, Y.; Ng, D.H.L.; Wang, G. Structure-Enhanced Removal of Cr(VI) in Aqueous Solutions Using MoS_2 Ultrathin Nanosheets. *New. J. Chem.* **2018**, *42*, 9006–9015. [CrossRef]
11. Wang, K.; Chen, P.; Nie, W.; Xu, Y.; Zhou, Y. Improved Photocatalytic Reduction of Cr(VI) by Molybdenum Disulfide Modified with Conjugated Polyvinyl Alcohol. *Chem. Eng. J.* **2019**, *359*, 1205–1214. [CrossRef]
12. Fageria, P.; Sudharshan, K.Y.; Nazir, R.; Basu, M.; Pande, S. Decoration of MoS_2 on g-C_3N_4 Surface for Efficient Hydrogen Evolution Reaction. *Electrochim. Acta* **2017**, *258*, 1273–1283. [CrossRef]
13. Qi, Y.; Liang, Q.; Lv, R.; Shen, W.; Kang, F.; Huang, Z.H. Synthesis and Photocatalytic Activity of Mesoporous g-C_3N_4/MoS_2 Hybrid Catalysts. *R. Soc. Open Sci.* **2018**, *5*, 180187. [CrossRef] [PubMed]
14. Samy, O.; el Moutaouakil, A. A Review on MoS_2 Energy Applications: Recent Developments and Challenges. *Energies* **2021**, *14*, 4568. [CrossRef]
15. Mamba, G.; Mishra, A.K. Graphitic Carbon Nitride (g-C_3N_4) Nanocomposites: A New and Exciting Generation of Visible Light Driven Photocatalysts for Environmental Pollution Remediation. *Appl. Catal. B Environ.* **2016**, *198*, 347–377. [CrossRef]
16. Zheng, D.; Zhang, G.; Hou, Y.; Wang, X. Layering MoS_2 on Soft Hollow g-C_3N_4 Nanostructures for Photocatalytic Hydrogen Evolution. *Appl. Catal. A Gen.* **2016**, *521*, 2–8. [CrossRef]

17. Huang, Q.; Liu, X.; Chen, Z.; Gong, S.; Huang, H. Surface Affinity Modulation of MoS_2 by Hydrothermal Synthesis and Its Intermediary Function in Interfacial Chemistry. *Chem. Phys. Lett.* **2019**, *730*, 608–611. [CrossRef]
18. Koutsouroubi, E.D.; Vamvasakis, I.; Papadas, I.T.; Drivas, C.; Choulis, S.A.; Kennou, S.; Armatas, G.S. Interface Engineering of MoS_2-Modified Graphitic Carbon Nitride Nano-Photocatalysts for an Efficient Hydrogen Evolution Reaction. *ChemPlusChem* **2020**, *85*, 1379–1388. [CrossRef] [PubMed]
19. Sivasankaran, R.P.; Rockstroh, N.; Kreyenschulte, C.R.; Bartling, S.; Lund, H.; Acharjya, A.; Junge, H.; Thomas, A.; Brückner, A. Influence of MoS_2 on Activity and Stability of Carbon Nitride in Photocatalytic Hydrogen Production. *Catalysts* **2019**, *9*, 695. [CrossRef]
20. Wei, H.; Zhang, Q.; Zhang, Y.; Yang, Z.; Zhu, A.; Dionysiou, D.D. Enhancement of the Cr(VI) Adsorption and Photocatalytic Reduction Activity of g-C_3N_4 by Hydrothermal Treatment in HNO_3 Aqueous Solution. *Appl. Catal. A Gen.* **2016**, *521*, 9–18. [CrossRef]
21. Tian, Y.; Ge, L.; Wang, K.; Chai, Y. Synthesis of Novel MoS_2/g-C_3N_4 Heterojunction Photocatalysts with Enhanced Hydrogen Evolution Activity. *Mater. Charact.* **2014**, *87*, 70–73. [CrossRef]
22. Visic, B.; Dominko, R.; Gunde, M.K.; Hauptman, N.; Skapin, S.D.; Remskar, M. Optical Properties of Exfoliated MoS_2 Coaxial Nanotubes—Analogues of Graphene. *Nanoscale Res. Lett.* **2011**, *6*, 593. [CrossRef] [PubMed]
23. Hu, K.H.; Hu, X.G.; Wang, J.; Xu, Y.F.; Han, C.L. Tribological Properties of MoS_2 with Different Morphologies in High-Density Polyethylene. *Tribol. Lett.* **2012**, *47*, 79–90. [CrossRef]
24. Konstas, P.S.; Konstantinou, I.; Petrakis, D.; Albanis, T. Synthesis, Characterization of g-C_3N_4/$SrTiO_3$ Heterojunctions and Photocatalytic Activity for Organic Pollutants Degradation. *Catalysts* **2018**, *8*, 554. [CrossRef]
25. Amini, M.; Ahmad Ramazani, S.A.; Faghihi, M.; Fattahpour, S. Preparation of Nanostructured and Nanosheets of MoS_2 Oxide Using Oxidation Method. *Ultrason. Sonochem.* **2017**, *39*, 188–196. [CrossRef]
26. Zhang, X.; Suo, H.; Zhang, R.; Niu, S.; Zhao, X.; Zheng, J.; Guo, C. Photocatalytic Activity of 3D Flower-like MoS_2 Hemispheres. *Mater. Res. Bull.* **2018**, *100*, 249–253. [CrossRef]
27. Thommes, M.; Kaneko, K.; Neimark, A.V.; Olivier, J.P.; Rodriguez-Reinoso, F.; Rouquerol, J.; Sing, K.S.W. Physisorption of Gases, with Special Reference to the Evaluation of Surface Area and Pore Size Distribution (IUPAC Technical Report). *Pure Appl. Chem.* **2015**, *87*, 1051–1069. [CrossRef]
28. Li, J.; Liu, E.; Ma, Y.; Hu, X.; Wan, J.; Sun, L.; Fan, J. Synthesis of MoS_2/g-C_3N_4 Nanosheets as 2D Heterojunction Photocatalysts with Enhanced Visible Light Activity. *Appl. Surf. Sci.* **2016**, *364*, 694–702. [CrossRef]
29. Barrera-Díaz, C.E.; Lugo-Lugo, V.; Bilyeu, B. A Review of Chemical, Electrochemical and Biological Methods for Aqueous Cr(VI) Reduction. *J. Hazard. Mater.* **2012**, *224*, 1–12. [CrossRef]
30. Du, X.; Yi, X.; Wang, P.; Deng, J.; Wang, C.C. Enhanced Photocatalytic Cr(VI) Reduction and Diclofenac Sodium Degradation under Simulated Sunlight Irradiation over MIL-100(Fe)/g-C_3N_4 Heterojunctions. *Cuihua Xuebao/Chin. J. Catal.* **2019**, *40*, 70–79. [CrossRef]